Geomorphology 357 (2020) 107104

Contents lists available at ScienceDirect

Geomorphology

journal homepage: www.elsevier.com/locate/geomorph

Spatial-temporal differentiation of eolian sediments in the Yarlung Tsangpo catchment, Tibetan Plateau, and response to global climate change since the Last Glaciation

Zhiyong Ling [a,b,*], Shengli Yang [b,**], Xin Wang [b], Jianping Wang [a], Dunsheng Xia [b], Fahu Chen [b,c]

[a] Key Laboratory of Comprehensive and Highly Efficient Utilization of Salt Lake Resources, Qinghai Provincial Key Laboratory of Geology and Environment of Salt Lake, Qinghai Institute of Salt Lakes, CAS, Xining 810008, China
[b] Key Laboratory of West China's Environmental Systems (Ministry of Education), College of Earth and Environmental Sciences, Lanzhou University, Lanzhou 730000, China
[c] Key Laboratory of Alpine Ecology, CAS Center for Excellence in Tibetan Plateau Earth Sciences and Institute of Tibetan Plateau Research, CAS, Beijing 100101, China

ARTICLE INFO

Article history:
Received 13 November 2019
Received in revised form 18 February 2020
Accepted 18 February 2020
Available online 19 February 2020

Keywords:
Eolian sediments
Quartz luminescence dating
Spatial-temporal differentiation
Paleoenvironment
Yarlung Tsangpo valley

ABSTRACT

Eolian sediments, an important paleoenvironmental archive, are widespread in the Yarlung Tsangpo River (YTR) valley of the southern Tibetan Plateau (TP), but their chronology and spatial-temporal differentiation are poorly understood. And it is not clear whether eolian accumulation is controlled by global climate changes, or local paleoenvironment, or both. In this study, we applied quartz OSL dating to 30 eolian sediment samples (sandy loess and eolian sand) from eight profiles in the YTR catchment. Our new dates were combined with 72 previously published eolian sediment ages (OSL/TL and ^{14}C) for the YTR catchment to analyze the response of eolian accumulation to paleoenvironmental changes. The overall dataset has eolian accumulation spanning the period from the Last Interglacial through to the Little Ice Age, ranging from 84.6 ± 8.7 ka BP (possibly as old as 118 ± 11 ka BP) to 0.4 ± 0.1 ka BP, with most occurring since the Late Glacial Period (15 ka BP), which suggests that the preservation of eolian deposits is controlled by geologic recirculation. Probability density function distributions (PDFs) of eolian ages from different parts of the YTR catchment show different age clusters, suggesting that factors controlling eolian accumulation vary across the catchment, so that spatial-temporal disparities are inherent in the system. To investigate the effect of regional and global paleoclimate since the Last Glacial Maximum (LGM) on eolian deposition processes in the YTR, we compared the PDF of ages from the combined dataset with a range of paleoclimate proxies. The PDF shows significant fluctuations since the LGM, including the Younger Dryas cold event. There is no consistent eolian sediment response to changes of the 30°N summer insolation, Asian Summer Monsoon, and westerlies. Phases of strong eolian sediment accumulation in the YTR basin do not show a simple correspondence with the classical global climate curve, suggesting that eolian processes in the alpine valley environment may be modified by local responses to these changes.

1. Introduction

The Yarlung Tsangpo River (YTR) basin is a major feature of the southern Tibetan Plateau (TP) that spans over 1500 km from west to east and contains a mix of broad valleys up to 30 km in width and deep canyons up to 2000 m depth (Yang et al., 1982; Yang, 1984). The YTR basin provides a significant volume of negative topography at the edge of the high plateau that is available for accumulation of eolian sediment, and eolian deposits are widely distributed in the basin, including eolian sand and sandy loess (Sun et al., 2007; Dong et al., 2017a, 2017b). In general, the sediments show a discontinuous zonal distribution along the valley of the YTR and its main tributaries, and are especially concentrated in the river-wide valley belt (Li et al., 1999; Lai et al., 2009; Kaiser et al., 2009). Eolian sediments in the YTR catchment are developed and deposited under the influence of climate and underlying surface conditions (Li et al., 1999), so are significant as indicators of regional climate and local environment and provide an important archive of climatic and environmental changes on the southern TP.

To date, eolian sediments in the YTR basin have been studied mainly from the perspectives of geomorphology (Yang, 1984; Li et al., 1997; Zhou et al., 2014), land use and land cover change (Shen et al., 2010, 2012; Li et al., 2016), provenance (Sun et al., 2007; Li et al., 2009; Du et al., 2018), sedimentary ages (Sun et al., 2007; Lai et al., 2009), and response to paleoenvironment (Jin et al., 1998; Lehmkuhl et al., 2000; Liu

* Correspondence to: Z. Ling, Key Laboratory of Comprehensive and Highly Efficient Utilization of Salt Lake Resources, Qinghai Provincial Key Laboratory of Geology and Environment of Salt Lake, Qinghai Institute of Salt Lakes, CAS, Xining 810008, China.
** Corresponding author.
E-mail addresses: lingzhiyong@foxmail.com (Z. Ling), shlyang@lzu.edu.cn (S. Yang).

https://doi.org/10.1016/j.geomorph.2020.107104
0169-555X/

et al., 2015; Stauch, 2015; Hu et al., 2018). The climate of the YTR basin on the southern edge of the TP is predominantly controlled by the interplay of the Asian summer monsoon (Indian monsoon and East Asian monsoon, ASM) and the westerlies (Böhner, 2006; Yao et al., 2012; Hou et al., 2017). Together, this climate pattern controls the hydrologic system, geologic cycles and geomorphologic processes, therefore, the response of eolian sediments to regional paleoclimate is complex. Along the 1500+ km length of the YTR in southern Tibet, prevailing climate conditions vary from semi-arid and arid in the upper reaches to humid in the middle and lower reaches (Dong et al., 2017b), therefore, there are likely to be spatial variations in the patterns of eolian sedimentary development and responses to paleoenvironment.

Previous studies on the chronology and paleoenvironment of eolian sediments in the YTR basin has focused on comparative study of single locations or small areas, mainly in individual areas within the catchment, with limited investigation of spatial-temporal differentiation of sedimentary development and response characteristics to different weather systems, the ASM and the westerlies, especially in middle reaches of the catchment. Further complexity is added by the potential influence of glacier erosion and meltwater since the Last Glacial Maximum (LGM). Results of published studies show that eolian sediments in this area mostly date to different periods between 21 and 3 ka BP (Lehmkuhl et al., 2000; Kaiser et al., 2009; Lai et al., 2009), with formed earlier (Jin et al., 1998, 2000), even dating back to the end of the early Pleistocene or early middle Pleistocene (Jin et al., 1998), with uncertainties. However, due to the complexities identified above, there is no agreement on the ages of the eolian sediments in the YTR catchment, which limits the understanding and interpretation of the past eolian processes and paleoenvironmental implications.

In this study we investigate the spatial and temporal distribution of eolian deposition in the middle reaches of the YTR valley in order to improve understanding of the chronology and implications of eolian deposits. First, we conduct quartz OSL dating for a set of new eolian samples located in areas from eight new profiles. We then combine our new ages with previously published data to allow comprehensive analysis of the dynamic mechanisms of formation and evolution eolian sedimentary development in different sections of the YTR valley. By comparing the chronology of eolian deposition with paleoclimatic proxies, we discuss the relationship between the eolian development processes and the regional paleoenvironment. Our study contributes to the establishment of a definitive chronology of eolian sedimentary deposition in the YTR catchment, improving our understanding of factors controlling eolian accumulation and the relationship between eolian sediment formation and development and the interplay of the ASM, the westerlies and the Tibetan winter monsoon.

2. Study area

The YTR originates from the Jemaangzong Glacier and is bounded by the Himalaya Mountains in the south and Gangdese-Nyainqentanglha Mountains to the north, with the regional terrain being high in the northwest and low in the southeast (Fig. 1). The YTR valley is beaded with canyons and wide valleys and multilevel terraces are formed by continuous downcutting. A diverse range of eolian sedimentary types are present in the valley (Fig. 2, Fig. 3), including eolian sand, sandy loess, and loess-like sediments (Li et al., 1997, 1999), and are mainly developed in wide reaches of the YTR such as the Maquan River wide valley, Xigaze wide valley, Lhasa-Sangri wide valley, and Mainlin wide valley, from west to east (Ling et al., 2019).

Maquan valley, the widest (20–30 km width) and highest (c. 4600 m asl) valley of YTR, located at the upper reaches of the catchment, has broad alluvial and lacustrine plains which are formed by braided rivers (Fig. 2A). In the valley, the annual rainfall ranges between 186 and 290 mm, and rainfall from June to September accounts for about 90% of this total, with a long dry period from October to May, corresponding to the seasons of winter and spring. In these seasons, the spread deposits of riverbeds and materials of wetlands are exposed to the prevailing southwest wind (Fig. 1C and D) and orographic wind to form eolian dunes which are mostly barchan dunes (Fig. 2A).

Xigaze valley, 5–8 km wide, with well-developed braids and flood plains, has different eolian deposits which are mainly distributed on the northern bank of the main stream of the YTR (Fig. 2B), concentrated on the alluvial fans and tributary valleys, a small number distributed on alluvial plains and hill slopes. On the southern bank, there is only a few sandy loess on the terraces and hill slopes. Lhasa-Sangri valley has a distance approximately 144 km from the west to the east, generally 3–5 km wide and the maximum width of 6 km (Dong et al., 2017b), which has the tributary of Lhasa River, being the largest in this region. Large and continuous area of sandy land or dunes are distributed on the northern bank of the YTR (Fig. 2C), with loess depositing at higher elevations on the hill slopes. Relatively a few of dunes and loess sediments are sparsely distributed on the southern bank. Both of the Xigaze valley and Lhasa-Sangri valley are mainly characterized by semi-arid climate, with elements of monsoon and semi-arid plateau climate (Dong et al., 2017b). Mean annual temperature is about 6–8 °C, with summer temperatures of >15 °C and winter temperatures below −2 °C and mean annual precipitation is 300–400 mm, mainly in July and August due to the ASM.

Mainlin valley, a lower and middle reaches of YTR catchment, extends from Mainlin County in the west to the town of Pai in the east, contained the lower part of the Niyang River, from Nyinchi city. Eolian deposits in this valley are mainly eolian dunes on the riverbeds or mountain slopes (Fig. 2D), and sandy loess on the terraces. The Mainlin wide valley is located in the southeast of the TP and is mainly affected by a semi-humid monsoon climate. Average annual temperature is 8.2 °C, with annual precipitation of ~650 mm, 85% of which is concentrated in June to September.

In short, larger areas of active eolian deposits controlled by the surface wind (Fig. 1C and D), can be found at the foot of the valley flanks and near tributary confluences in the above wide valleys. And the terraces, riverbed, and piedmont are covered by differing thicknesses (average c. 2.5–10 m) of eolian sediments (Ling et al., 2019), apart from areas of scree and bare rock, and active fluvial and peat bog sites.

3. Methods

3.1. Data collection and sampling

To understand the spatial-temporal differentiation of eolian sedimentary development in different regions of the YTR valley, eight new sections were selected for OSL dating and the results combined with eolian sediments ages from 27 previously published profiles as collated in Ling et al. (2019). The new sections were chosen to fill in gaps in the existing record in the wide valley from Xigaze to Mainlin of the middle YTR valley where the published data on the eolian sediment is relative paucity, and the combined dataset extends over c. 1500 km from west to east (Fig. 1), spanning the different climate zones from arid to monsoon-influenced (Dong et al., 2017b).

The seven new eolian sediment sections and one lacustrine deposit section, with different sedimentary characteristics (Fig. 3), were selected on the basis of good exposures through sequences and to enable a good geographic spread. A total of 36 OSL samples were taken from the sections (Fig. 5, Table 1), comprising 30 of eolian sediment (eolian sand or sandy loess) and 6 from other sedimentary contexts (one sample each from a transition layer (YJP1) and fluvial sandy clay (LCP), two fluvial samples from section YJP1, and two lacustrine samples from PLP). Samples were collected by driving iron tubes (25 cm in length and 4 cm in diameter) into the freshly prepared section. The ends of each tube were covered by a ball of seedless cotton when the tube was filled with sediments, and then wrapped with opaque plastic tape.

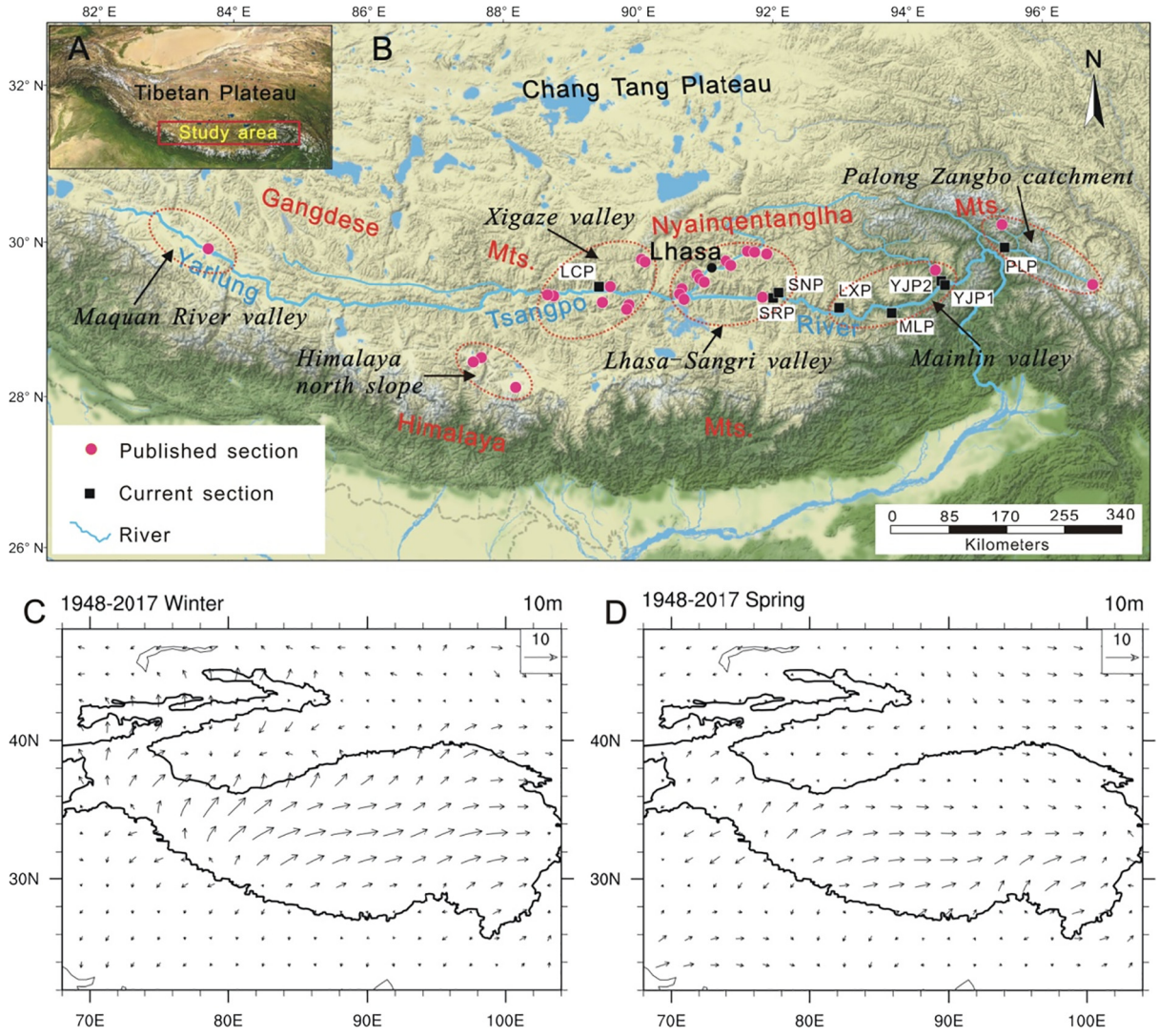

Fig. 1. Location of the study area, sampling sites and wind regime of the TP and its adjacent area. (A) Location of the YTR valley on the TP; (B) Location of the six eolian sediment sampling areas used in this study (shown with red dotted lines). (C, D) Ground wind (10 m above the surface) in winter and spring of the TP and its adjacent area (The solid line is extracted with MeteoInfo at 2000 m asl. The YTR valley is near 30°N. The wind data is downloaded from https://www.esrl.noaa.gov/psd).

The previously published eolian sediment ages from the YTR catchment were taken from Ling et al. (2019) who collated data from a number of studies (e.g., Li et al., 1999; Lehmkuhl et al., 2000; Sun et al., 2007; Kaiser et al., 2009; Lai et al., 2009; Liu et al., 2015; Hu et al., 2018). A total of 72 ages were selected, determined using OSL/TL and conventional and AMS ^{14}C methods, and combined with OSL ages from the 30 new eolian samples to give a total dataset of 102 ages. The ages were analyzed using a probability density function (PDF) method as previously employed for OSL age distribution analysis (Lai et al., 2009; Stauch, 2015; Chen et al., 2016). The PDF was calculated for each eolian sediment age based on its mean and the standard deviation. The individual PDFs then were summed as a cumulative PDF. In this approach, each eolian sediment date is treated as an individual accumulation event (Singhvi et al., 2001; Telfer and Thomas, 2007), so the cumulative PDF can be considered as representing the trend of eolian conditions that is indicative of paleoenvironment.

3.2. OSL dating

An automated Risø TL/OSL-DA-20 reader for TL/OSL dual-purpose dating, equipped with a ^{90}Sr/^{90}Y beta source, produced in the Danish Risø Laboratory, was used for OSL measurements in the optical luminescence laboratory of Qinghai Institute of Salt Lakes, CAS. The signal was stimulated by blue diodes ($\lambda = 470 \pm 20$ nm) at 130 °C for 40 s, and a Hoya U-340 (7.5 mm) filter, placed in front of the photomultiplier tube (9235QA), was used for detection and recording.

Single aliquot regenerative-dose (SAR) technology was employed for the equivalent dose (De) determination of the quartz grains (Murray and Wintle, 2000). The De, tested using medium size (38–63 μm) quartz, suitable for De determination of eolian sediments (Ling et al., 2018), extracted from the sediments of all sections, was estimated by interpolation of the natural luminescence signal onto the growth curve. The growth curves were constructed using regeneration doses, including a dose of 0 Gy for monitoring the thermal transfer effect and a repeated first regeneration dose for checking the accuracy of the sensitivity correction. A fixed, small test dose after the natural and regenerative OSL measurements was used to adjust the sensitivity. At the end of the protocol, the sample was dosed and tested for feldspar contamination (Lai et al., 2009). The preheat temperature for natural and regenerative doses of samples was 260 °C for 10 s, and cut-heat was set at 220 °C for 10 s. The first 1.6-s integral of the primary OSL signal, minus a

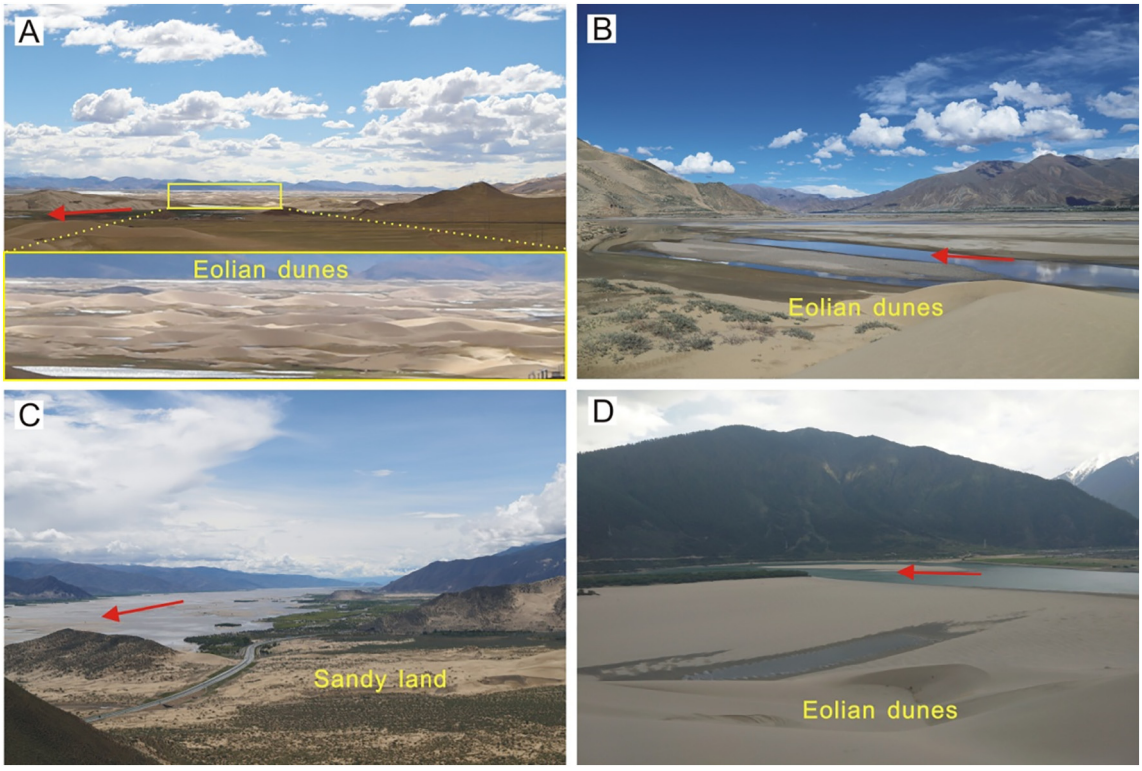

Fig. 2. Landform of the wide valley and eolian sediments in different reaches of YTR. (A) Eolian dunes in the wide valley of Maquan River; (B) Eolian dunes on the terrace and sand on the riverbed in Xigaze wide valley; (C) Sandy land on the north bank in Lhasa-Sangri wide valley; (D) Sand on the riverbed and eolian dunes at the hill slope in the Mainlin wide valley. The red arrows indicate the direction of the river (from west to east).

background signal estimated from the last 8-s integral (Jin et al., 2018), was used for De estimation.

The concentrations of U, Th, and K were measured by ICP-MS at the Chemical Analysis Laboratory of Qinghai Institute of Salt Lakes. The contribution of cosmic rays to the annual dose was calculated from the altitude, geographical location, and sampling depth of the samples (Prescott and Hutton, 1994). For the 38–63 μm quartz grains, an alpha efficiency factor of 0.035 ± 0.003 was assumed to estimate the alpha contribution to the dose rate (Lai and Brückner, 2008). The parameters used to calculate the annual dose were based on the standards provided by Aitken (1998) and are shown in Table 1. Long-term water content was assumed to be 10 ± 5% and was added to each value in the age calculations.

4. Results

4.1. Luminescence characteristics

Examples of shine-down curves and growth curves for typical samples (YJP1–3, SNP-3 and SNP-4) are shown in Fig. 4. The OSL signal decreases very quickly within the first second of stimulation, suggesting that quartz OSL signal is dominated by the fast component (Fig. 4a, c and e). The growth carve was fitted using a single saturation exponential plus linear function. There is clearly a linear growth part in the growth curve beyond a regeneration dose of 40 Gy for YJP1 (Fig. 4b), and 500 Gy for SNP (Fig. 4d), which may allow for determination to a higher dose range (Lai et al., 2009). But for some loess samples, the growth curve has stopped growing at a regeneration dose of 320 Gy (Fig. 4f) which is greater than twice the value of D0, thereby suggesting that the quartz signal is saturated for testing. This may indicate an underestimation of the OSL age for old loess samples, so maybe we can only get the minimum age of the loess deposition. Additionally, according to the dating results of SNP-3 and SNP-4 (Table 1), the limit age of quartz used in the sandy loess from YTR catchment is about 60–70 ka BP.

For all samples, to evaluate the conditions of the OSL test, a zero-dose cycle was incorporated in the SAR protocol to test the effect of thermal transfer. The decay curve of 0 Gy regeneration dose shows negligible thermal transfer. And the recycling ratios are consistent to within 10% of unity (0.9–1.1) for all samples.

4.2. Timing of eolian sediment deposits

Luminescence dating results for the 36 new samples are summarized in Table 1; ages are listed by profile and depth (Fig. 5). The 30 OSL ages for eolian samples range from 0.4 ± 0.1 ka BP in profile SRP to at least 84.6 ± 8.7 ka BP in profile SNP. This suggests that eolian sediment started from the last interglacial period through to at least the little ice age, if not the present day. The date range of eolian deposition from the Late Pleistocene to the Holocene corresponds with results from previous studies (Kaiser et al., 2009; Lai et al., 2009).

Ten of the 36 OSL ages in Table 1 are older than 56 ka BP. Most of the older dates are from loess sediments (profile SNP), but two are from lacustrine deposits (profile PLP), suggesting that different parts of the YTR catchment may have different sediment responses in the same geologic period. The loess ages from SNP range from c. 57–85 ka BP, but as they are close to the saturation limit for quartz OSL dating, their actual ages may be older. Hence, it is likely that loess deposition commenced earlier in MIS 5, during the last interglaciation. OSL ages for eolian sand (profiles MLP and SRP) mainly date to the mid- to late Holocene, which is later than sandy loess/loess sediment deposition. The differentiation in ages of eolian

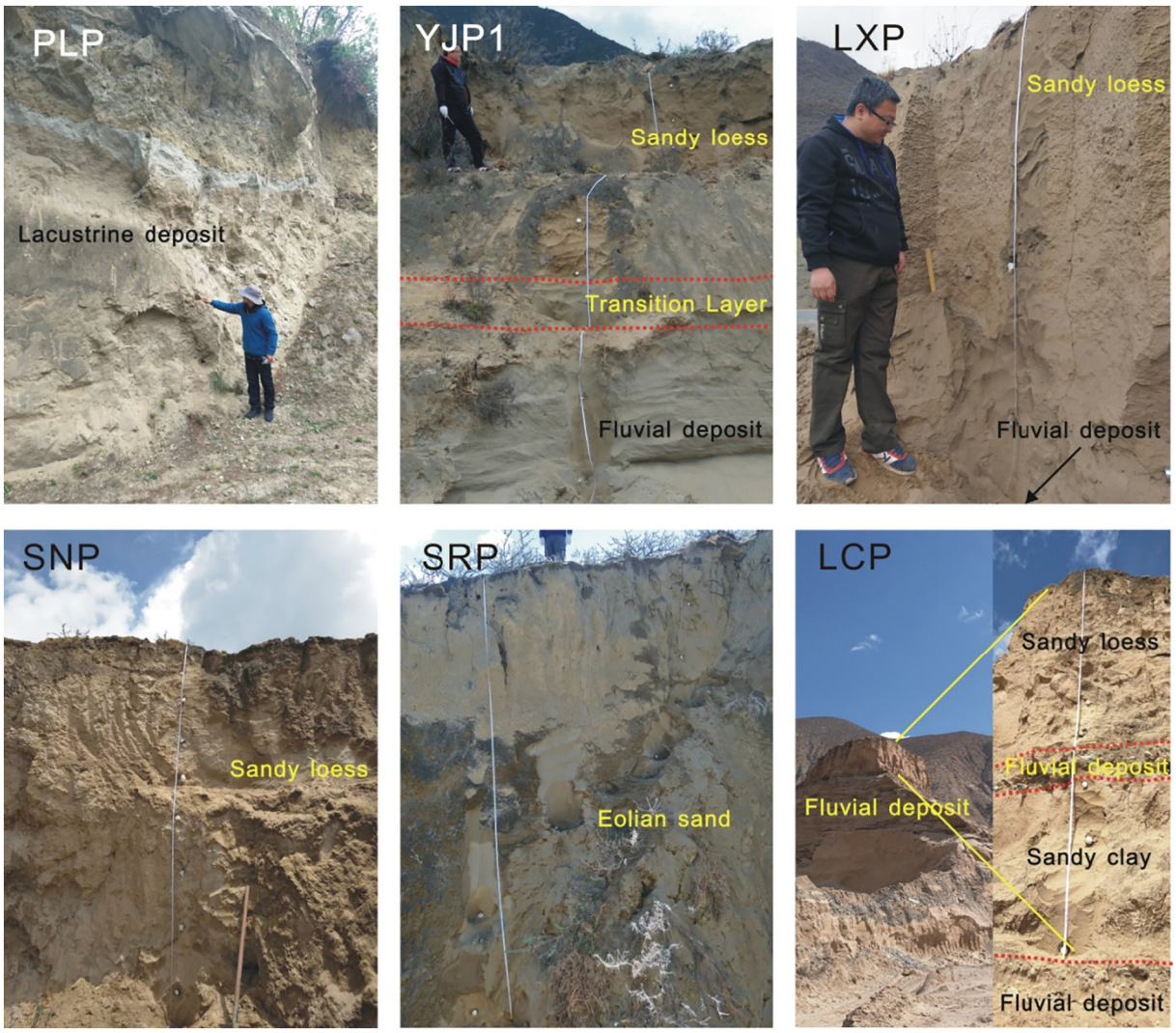

Fig. 3. Photos of main sections and their sedimentary characteristics investigated in the study. See Fig. 1 for their locations.

sand and loess in the YTR catchment has also been identified by Lai et al. (2009), but no specific explanation was given.

Most of the 72 eolian sediment ages from Ling et al. (2019) date to Marine Isotope Stage 3 (MIS 3) (Johnsen et al., 2001) or later, especially since the late glacial period (15 ka BP). The youngest eolian sediment age is c. 0.4 ka BP. Only eight ages pre-date MIS 3, two are from MIS 4 and six from MIS 5, with the oldest at 118 ± 11 ka BP (Lai et al., 2009). The older OSL ages are concentrated in four profiles adjacent to the Lhasa River valley, a north bank tributary of the YTR (Fig. 1).

4.3. Spatial-temporal distribution of sedimentary ages

Fig. 6 displays the temporal and spatial distribution of the 102 eolian sediment ages from the combined dataset. The overall temporal distribution of the data (Fig. 6a) shows a concentration of eolian sediment ages since MIS 3 (~50 ka BP), especially after MIS 1 (~14 ka BP) where there are 70 ages accounting for c. 69% of the total. The spatial distribution (Fig. 6b) shows a concentration of eolian sediment age samples in the Lhasa-Sangri wide valley, the Xigaze valley, and the Mainlin valley, which together account for c. 80% of the total. The spatial concentration of samples may reflect the different priorities of eolian research in the catchment. However, overall the spatial-temporal distribution of sedimentary ages in the YTR catchment is uneven.

4.4. Age distribution for different deposits

The analysis of 102 ages, including sand, sandy loess/loess and paleosols indicates a main phase of eolian accumulation in the YTR catchment since LGM, and c. 80% in younger than ~50 ka BP. Therefore, the analysis of the PDFs for the different deposits ages focuses on the time since 50 ka BP (Fig. 7). The PDF of sand suggests that eolian accumulation was dominant since the Holocene, with three periods of <11–6 ka BP, 5–2 ka BP and since 2 ka BP, but has a hiatus at 2 ka BP. And it also indicates an eolian accumulation period of 26–13 ka BP, corresponding to the LGM roughly. In the YTR catchment, loess accumulation concentrated in two phases from 48 ka BP to 28 ka BP and from 16 ka BP to 2 ka BP, which has no existing during the LGM (c. 26–16 ka BP) and after 2 ka BP. From eolian deposits in which paleosols were not developed only 14 ages are available which distributed in short periods during the phases of the loess accumulation. The ages span the time about 13 ka BP, 8 ka BP and between 6 ka BP and 2 ka BP with a gap at c. 4 ka BP.

In the YTR basin, enhanced loess accumulation began a little earlier than the eolian deposition, but its fluctuation was not as severe as the

Table 1
Summary characteristics and OSL ages for the 36 new analyses undertaken in this study.

Lab. no.	Sample ID[a]	Coordinates	Altitude (m)	Depth(m)	Th (ppm)	U (ppm)	K (%)	Dose rate(Gy/Ka)	De (Gy)	OSL age (ka)
01	**PLP-01**	29°58′04.1″N,95°21′48.9″E	2562	4.5	18.12 ± 0.6	1.93 ± 0.3	2.25 ± 0.05	4.14 ± 0.27	233.9 ± 28.7	56.5 ± 8.5
02	**PLP-02**			8.0	16.21 ± 0.8	2.52 ± 0.4	2.92 ± 0.04	4.55 ± 0.34	268.2 ± 33.0	58.9 ± 8.5
03	YJP1–1	29°27′20.2″N,94°28′09.5″E	2943	0.4	15.06 ± 0.8	1.45 ± 0.3	2.05 ± 0.04	3.62 ± 0.26	6.8 ± 0.1	1.9 ± 0.1
04	YJP1–2			0.9	15.23 ± 0.8	1.65 ± 0.3	2.04 ± 0.04	3.65 ± 0.26	14.2 ± 0.2	3.9 ± 0.3
05	YJP1–3			1.4	15.28 ± 0.8	1.73 ± 0.3	2.05 ± 0.04	3.66 ± 0.27	16.2 ± 0.2	4.4 ± 0.3
06	YJP1–4			1.9	15.69 ± 0.8	1.93 ± 0.3	2.09 ± 0.04	3.76 ± 0.27	16.0 ± 0.2	4.3 ± 0.3
07	YJP1–5			2.5	17.60 ± 0.8	1.80 ± 0.3	2.23 ± 0.04	3.97 ± 0.29	20.4 ± 0.4	5.1 ± 0.4
08	YJP1–6			3.0	17.05 ± 0.8	1.92 ± 0.3	2.13 ± 0.04	3.85 ± 0.28	12.5 ± 0.2	3.2 ± 0.2
09	YJP1–7			3.6	18.22 ± 0.8	3.64 ± 0.4	2.17 ± 0.04	4.41 ± 0.32	36.6 ± 1.0	8.3 ± 0.6
10	**YJP1–8**			4.3	15.95 ± 0.8	2.94 ± 0.4	2.24 ± 0.04	4.10 ± 0.30	36.8 ± 3.5	16.3 ± 1.5
11	**YJP1–9**			4.8	11.87 ± 0.7	2.00 ± 0.4	2.17 ± 0.04	3.48 ± 0.27	56.8 ± 4.3	16.3 ± 1.8
12	**YJP1–10**			5.6	10.10 ± 0.7	2.01 ± 0.4	2.19 ± 0.04	3.36 ± 0.26	84.1 ± 3.5	25.1 ± 2.2
13	YJP2			1.7	10.94 ± 0.7	1.64 ± 0.3	2.07 ± 0.04	3.34 ± 0.24	36.8 ± 1.0	11.0 ± 0.9
14	MLP-1	29°07′08.0″N,93°46′41.0″E	3004	6.5	13.56 ± 0.7	1.74 ± 0.3	2.07 ± 0.04	3.42 ± 0.26	15.3 ± 0.2	4.5 ± 0.3
15	MLP-2			10.0	12.90 ± 0.7	1.77 ± 0.3	2.11 ± 0.04	3.37 ± 0.26	20.7 ± 0.3	6.2 ± 0.5
16	LXP-1	29°04′00.4″N,92°47′57.7″E	3172	1.3	12.51 ± 0.7	1.90 ± 0.3	2.34 ± 0.04	3.76 ± 0.27	18.6 ± 0.2	4.9 ± 0.4
17	LXP-2			2.0	10.09 ± 0.7	1.32 ± 0.3	2.42 ± 0.04	3.48 ± 0.26	22.6 ± 0.5	6.5 ± 0.5
18	SNP-1	29°16′53.3″N,91°56′59.6″E	3598	0.6	17.07 ± 0.8	1.90 ± 0.3	2.26 ± 0.04	4.10 ± 0.29	257.9 ± 16.5	62.9 ± 6.0
19	SNP-2			1.1	18.02 ± 0.8	1.95 ± 0.3	2.26 ± 0.04	4.15 ± 0.29	236.3 ± 29.5	56.9 ± 8.2
20	SNP-3			1.7	24.30 ± 0.9	2.58 ± 0.4	2.21 ± 0.04	4.71 ± 0.34	270.9 ± 13.9	57.5 ± 5.1
21	SNP-4			2.2	25.23 ± 0.9	2.37 ± 0.4	2.34 ± 0.04	4.82 ± 0.35	358.8 ± 20.2	74.5 ± 6.8
22	SNP-5			2.7	18.77 ± 0.8	2.31 ± 0.4	2.17 ± 0.04	4.42 ± 0.32	308.8 ± 13.2	69.8 ± 5.9
23	SNP-6			3.2	36.29 ± 0.9	2.69 ± 0.4	2.23 ± 0.04	4.95 ± 0.42	290.9 ± 15.9	58.8 ± 5.4
24	SNP-7			3.7	29.45 ± 0.9	2.56 ± 0.4	2.45 ± 0.04	5.57 ± 0.40	328.5 ± 24.4	59.0 ± 6.1
25	SNP-8			4.2	25.08 ± 0.9	2.71 ± 0.4	2.44 ± 0.04	4.25 ± 0.31	359.2 ± 26.3	84.6 ± 8.7
26	SRP-1	29°15′42.0″N,91°59′14.2″E	3553	0.7	14.18 ± 0.7	2.07 ± 0.4	2.16 ± 0.04	4.06 ± 0.30	1.7 ± 0.1	0.4 ± 0.1
27	SRP-2			1.4	15.36 ± 0.8	2.05 ± 0.4	2.22 ± 0.04	4.18 ± 0.31	3.4 ± 0.1	0.8 ± 0.1
28	SRP-3			2.1	17.30 ± 0.8	1.81 ± 0.3	2.29 ± 0.04	4.29 ± 0.31	4.2 ± 1.1	1.0 ± 0.1
29	SRP-4			2.8	17.20 ± 0.8	1.97 ± 0.3	2.24 ± 0.04	4.26 ± 0.31	4.7 ± 0.1	1.1 ± 0.1
30	SRP-5			3.5	20.13 ± 0.9	2.22 ± 0.4	2.24 ± 0.04	4.53 ± 0.34	4.6 ± 0.1	1.0 ± 0.1
31	SRP-6			4.2	16.52 ± 0.8	2.14 ± 0.4	2.29 ± 0.04	4.26 ± 0.32	5.2 ± 0.2	1.2 ± 0.1
32	SRP-7			4.9	14.82 ± 0.7	1.83 ± 0.4	2.35 ± 0.04	4.07 ± 0.30	16.9 ± 1.0	4.1 ± 0.4
33	LCP-1	29°23′13.9″N,89°19′31.6″E	3815	2.9	16.21 ± 0.7	2.41 ± 0.4	2.61 ± 0.04	4.60 ± 0.34	42.5 ± 1.6	9.2 ± 0.8
34	LCP-2			3.6	17.08 ± 0.9	2.32 ± 0.4	2.62 ± 0.04	4.58 ± 0.34	53.4 ± 2.1	11.7 ± 1.0
35	LCP-3			4.2	20.96 ± 0.8	2.75 ± 0.4	2.64 ± 0.04	5.12 ± 0.37	68.8 ± 2.8	13.6 ± 1.1
36	**LCP-4**			6.1	14.09 ± 0.7	2.49 ± 0.4	2.53 ± 0.04	4.36 ± 0.33	47.8 ± 2.0	11.0 ± 0.9

Water content was taken as 10 ± 5% for all samples. The ID of non-eolian samples are distinguished in bold.
[a] Three letter codes relate to sample site location as shown in Fig. 1.

sand. The correspondence of paleosol with the trough of loess and sand, or a short occurrence in the continuous process of loess accumulation, may indicate the short relative climatic optimum period when the eolian deposits in the YTR catchment. On the whole, the PDFs of the three type sediments show that they enhanced since LGM, which is dominated by eolian sediments in the YTR basin. At the present state, there are no enough data of different eolian types for the six different wide valleys. Therefore, the PDFs of the three eolian types are only analyzed for the whole catchment.

5. Discussion

5.1. Comparison of age distribution in different regions

Because of the same material source (Li et al., 2009; Du et al., 2018), the sand, loess/sandy loess and paleosol are all considered as eolian deposits to analyzed their ages distribution collectively. Fig. 8 shows PDFs of eolian sediment ages for six different regions of the YTR catchment using the combined dataset. There are clear differences between the PDF curves. In the Maquan River, Himalaya north slope, Mainlin, and Palong Zangbo valleys there are marked peaks (age clusters) from the early Holocene, mainly since 8.5 ka BP, while eolian deposition in Xigaze valley dates back to 17 ka BP, and there are three age clusters in the Lhsasa-Sangri valley since c. 100 ka BP (at about ~11, 12–40, and 44–96 ka BP). The Maquan River, Lhasa-Sangri, and Mainlin valleys display a hiatus in eolian accumulation since 2 ka BP, which may be related to regional erosion. Other YTR valleys have eolian depositional hiatuses at different times; c. 9–15 ka BP in Maquan River, 9–12 ka BP for the north slope of the Himalaya Mountains, 13–24 ka BP in Mainlin valley and 8.3–18 ka BP in the Palong Zangbo River catchment. These differences suggest that the factors governing eolian accumulation processes may be different in each valley, making spatial-temporal disparities inherent.

Based on OSL dating of samples from the Xigaze valley and analysis of previously published dating results, Sun et al. (2007) suggested that loess deposition in YTR valley commenced after the Last Deglaciation, with a hiatus during the LGM period due to erosion of loess as glaciofluvial outwash. Outwash erosion may explain the lack of LGM eolian deposition in other glacial regions of the YTR catchment, for example, the Himalaya north slope, Mainlin valley, and Palong Zangbo valley. Another factor that may have contributed to the lack of preservation of early eolian deposits is the development of a dammed lakes in the YTR valley. Hu et al. (2018) identified three paleo-lake sedimentary sequences on terraces in the broad Xigaze valley dating from 13 to 30 ka BP, at a lake altitude of 3811 m asl. A similar phenomenon was identified by Liu et al. (2015) in the Mainlin valley, indicating the presence of a paleo-lake at 3180 m asl during the last glacial period (~41–13 ka BP). Loess deposits on a platform on the eastern mountain of Nyingchi in the Mainlin valley were less affected by erosion due to their high elevation (3303 m asl, about 300 m above the modern river), and provide dates to c. 40 ka BP (Liu et al., 2015).

The older eolian deposits are well preserved in the Lhasa-Sangri wide valley, showing that eolian accumulation took place in the Last Glaciation, and also during the Last Interglaciation. The preservation of older eolian deposits points to a lack of erosion by glacier ice and outwash during the LGM and supports the view of previous studies

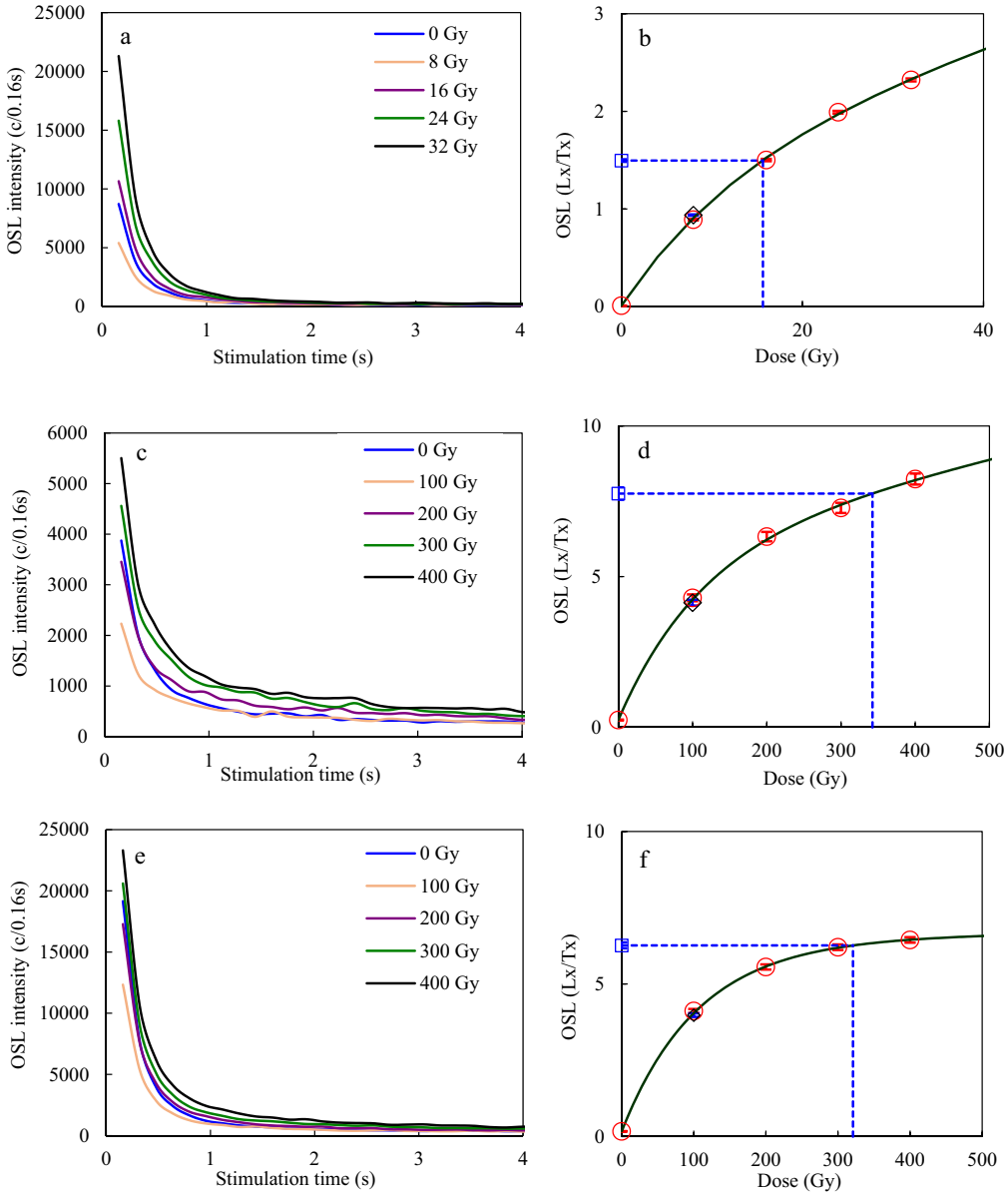

Fig. 4. Representative OSL characteristics for medium-grained (38–63 μm) quartz. (a, c, e) Shine-down curves for samples YJP1-3 (a), SNP-3 (c), and SNP-4 (e); (b, d, f) Growth curves for samples YJP1-3 (b), SNP-3 (d), and SNP-4 (f).

(Zhang and Li, 2002; Lai et al., 2009) that an ice sheet did not extend over the whole TP at the LGM, and that not all pre-Holocene loess deposits were removed during Deglaciation.

The contrasting patterns of loess preservation and/or erosion in different parts of the YTR catchment show a strong dependence on local environmental conditions. In general, fewer early eolian sediments are preserved in those areas where conditions were insufficient due to geologic recirculation (e.g., erosion effect, deposition-reactivation-redeposition process). Long-term accumulation of eolian sediments is controlled by favorable sedimentary environment (e.g., suitable climate for eolian deposition, abundant provenance) and local preservation conditions in the area of deposition (e.g., Lancaster, 2008; Chase, 2009).

5.2. *Environmental implications of eolian sediments in the YTR catchment*

The accumulation of the eolian sediments may be controlled by several, sometimes interacting factors: local topography and landforms (e.g., Mason et al., 1999; Ling et al., 2019), changes in surface roughness, e.g., due to vegetation cover (Sun et al., 2007; Stauch, 2015), and climate-induced changes in wind speed (e.g., Roskin et al., 2011). There are different interpretations of the role of climatic factors in controlling the accumulation of eolian sediments on the TP. Typically, sand accumulation is considered as representative of an arid climate period in deserts and in arid and semi-arid areas (Lai et al., 2009; Stauch, 2015). However, the YTR valley spans a significant distance from west to east and areas of eolian deposition (Li et al., 1997; Li et al., 1999) encompass extremely complex geomorphological settings such as canyons, wide valleys, fluvial/alluvial fans (Li et al., 1999) and different climate types, e.g., semi-humid, semi-arid, and arid (Dong et al., 2017a, 2017b). Therefore, eolian sediments formed in different parts of the catchment may have different indicative meanings for paleoenvironmental interpretation, and the process of sedimentary development may not simply reflect a regional arid climate as in the northern desert of China.

The main sources of eolian sediments on the TP are glacial outwash material (Sun et al., 2007; Smalley et al., 2014) as well as

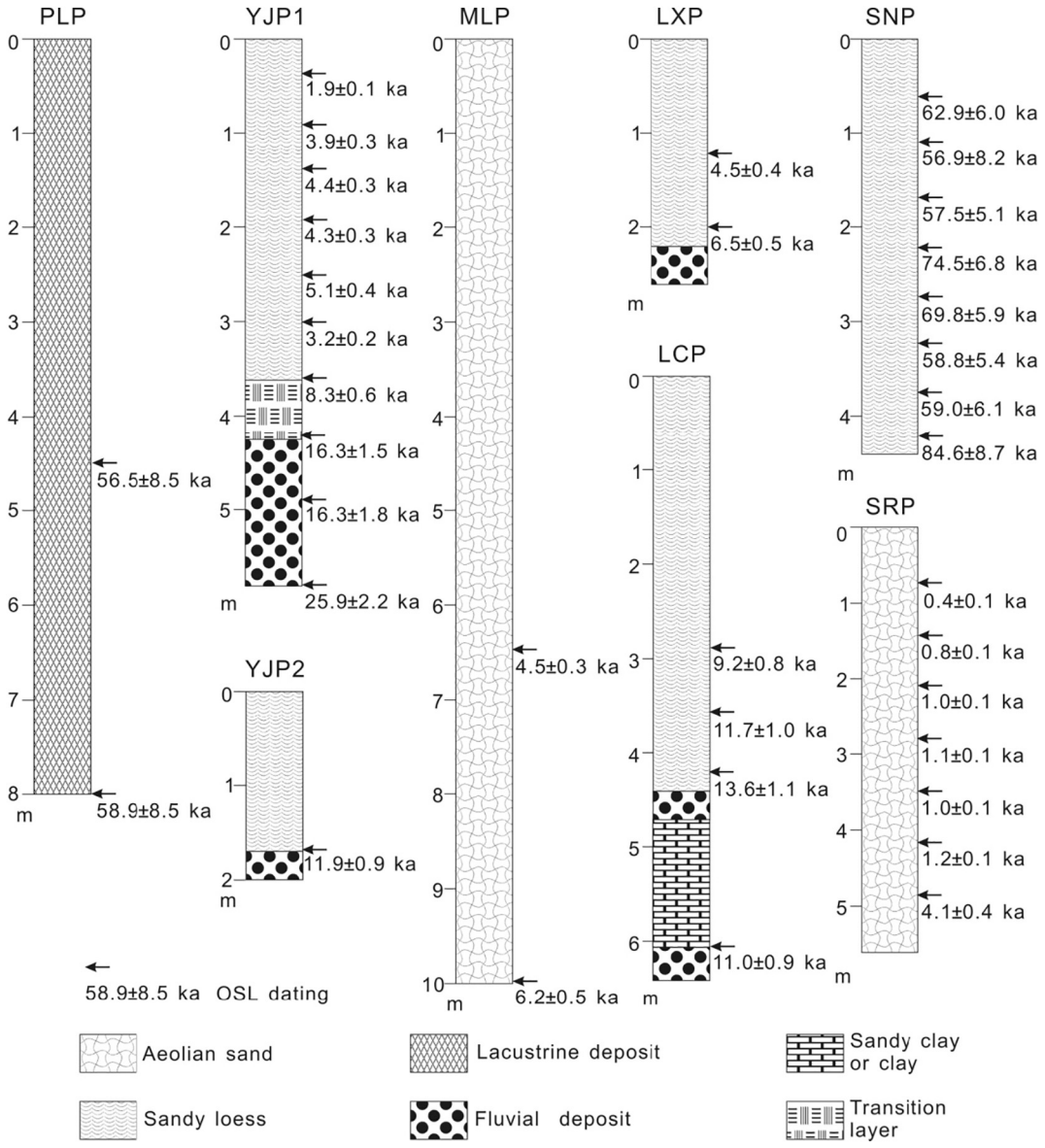

Fig. 5. Sediment logs and geochronological data for profiles investigated in the study. See Fig. 1 for locations.

fluvial/alluvial deposits and dried lake basins (Kaiser et al., 2010; Pan et al., 2013; Stauch et al., 2014). Under the same provenance, different types of eolian sediment (sand, loess, etc.) may be deposited in different reaches of the YTR, depending in altitude, wind strength, and underlying surface conditions. Additionally, eolian sediments are widely distributed across different climatic regions of the YTR catchment, including more humid locations such as Mainlin and Nyingchi with an annual precipitation of c. 600–700 mm. Therefore, eolian deposition in the YTR catchment cannot simply be correlated with aridity to indicate an arid paleoenvironment. The climatic and

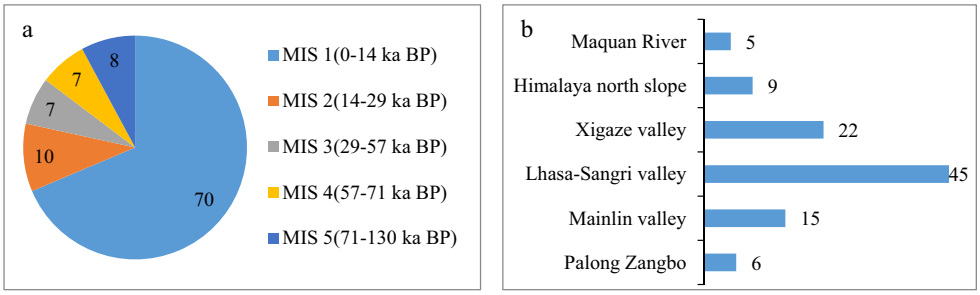

Fig. 6. Spatial and temporal distribution of eolian sediment ages, based on 102 samples (30 from the current study and 72 from previously published studies). (a) Pie chart showing number of sample ages in different climatic stages (corresponding to the Marine Isotope Stages (MIS) 1 to 5) (Johnsen et al., 2001); (b) distribution of samples in different areas of the YTR catchment. See Fig. 1 for locations.

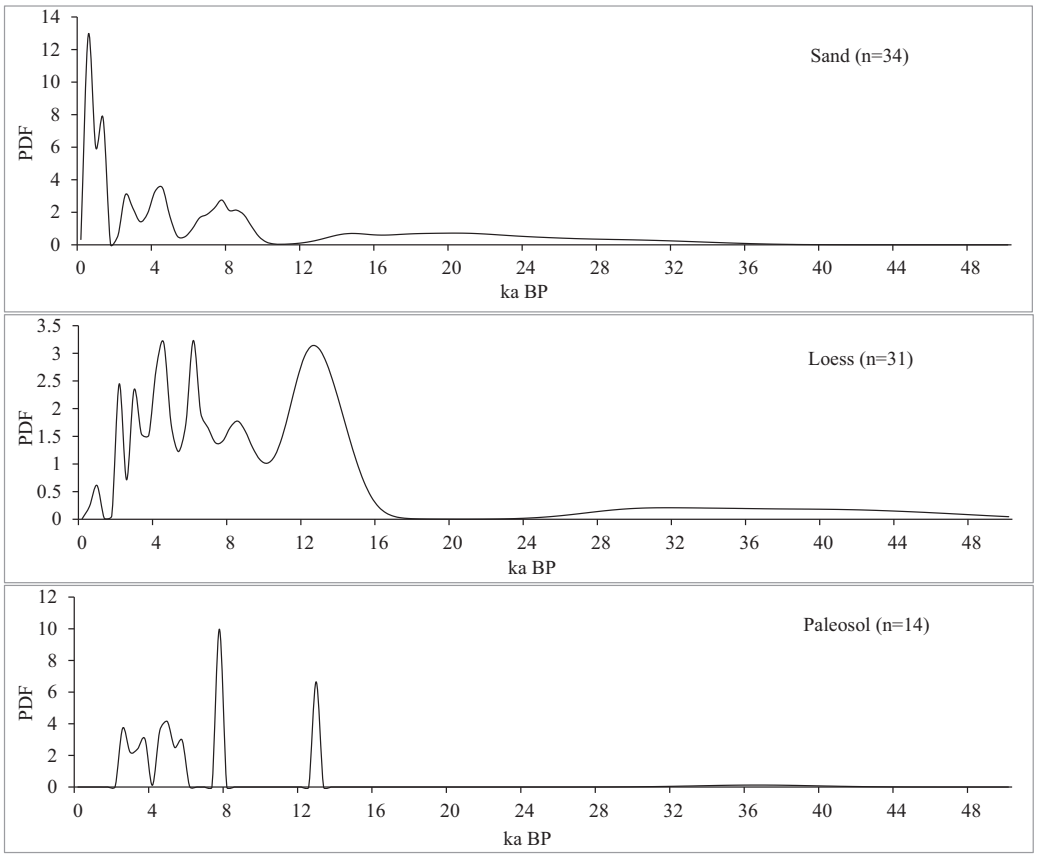

Fig. 7. Probability density functions (PDFs) of different eolian deposits (sand, loess/sandy loess and paleosol) ages in the YTR catchment.

environmental conditions indicated by eolian deposits in different developmental reaches in the YTR valley should be treated differently. Eolian deposition in the middle-upper reaches of the YTR may respond to variations in the strength and interactions of the ASM and westerlies. In the middle-lower reaches, eolian deposition is more likely to be generated by ASM superimposed with local environment, underlying surface roughness, and other factors (such as topography, vegetation, valley fog-wind and glacier wind), and the deposition process may also record enhanced ASM signals (Ling et al., 2019).

5.3. *Drivers of eolian processes since 50 ka BP*

Fig. 9 plots the PDF for the combined dataset of 102 ages for eolian sediment accumulation in the YTR catchment with various indicators of paleoclimate since 50 ka BP. We have restricted the time period to 50 ka as evidence for eolian deposition prior to this is patchy and equivocal. In general, the PDF curve shows little change until the LGM, after which it gradually increases to a peak after 15 ka BP, with more marked fluctuations thereafter (Fig. 9A), indicating enhancement in the intensity of eolian accumulation. This pattern of eolian activity is similar to that identified in other areas of the TP (Stauch, 2015). In the catchment, the proximity to fluvial sources for the majority of the deposits suggests that sediment supply from fluvial sources is likely a major driver of sediment accumulation (Jin et al., 1998). Deglaciation of the Himalaya Mountains or Gandese Mountains may be a significant source of material, as indicated by the peak in number of ages after 15 ka, agreeing with the results of the rain shadow zone of the Indian Summer Monsoon where sand ramps distribute on south slope of Himalaya Mountains (Kumar et al., 2017).

Additionally, the YTR catchment PDF has a good record of the Younger Dryas (YD) event (Tarasov and Peltier, 2005), which is consistent with the record from other eolian proxies elsewhere on the TP, such as nebkha dunes development in the northeast (Ling et al., 2018). These similarities indicate that different types of eolian deposition on the plateau may show synchronized response to paleoclimate since the LGM. However, when the PDF of eolian sediment ages in the YTR catchment is compared with other paleoclimate indicators (Figs. 9B–E), there appears to be no simple correspondence between periods of strong accumulation and global climate events, but a more complex response pattern (Fig. 9). In part, this is due to inherent spatial-temporal complexities in the nature of the eolian record and its response to paleoclimate, as highlighted by Lancaster et al. (2013) with respect to eolian deposition in deserts. The varied geomorphology of the YTR basin and the influence of different wind systems means that the relationship between eolian deposition and paleoenvironmental conditions is potentially more complex. Other factors, such as the uplift of the TP, introduced spatial-temporal complexity in the intensity and location of weather systems (ASM, westerlies) in the Quaternary (Jin et al., 1998, 2000). As the Plateau uplift, the abundant clastic materials in the YTR basin provided a source for regional eolian deposition. Meanwhile the uplift plateau also reduced the influence of the ASM and contributed to the dry and cold climate conditions needed for the development of eolian accumulation. By c. 80 ka BP, the TP had risen to nearly its modern height, and the modern atmospheric circulation pattern had been basically established. The fault valley of the YTR was formed in the uplift process of the plateau, giving rise to the alpine canyon landscape and geomorphic complexity (Wang et al., 2014) that affect processes and location of eolian accumulation in the valley. For example, the valley slope is concave and convex in middle and lower reaches and the valley is narrow and curved. Here, eolian deposition may be controlled more by local environmental factors such as topography and vegetation rather than regional climate. Lake records on the TP suggest that the ASM was at its weakest in the late Pleistocene (20–11 ka BP) (Hou et al., 2017), but did extend to 30°N.

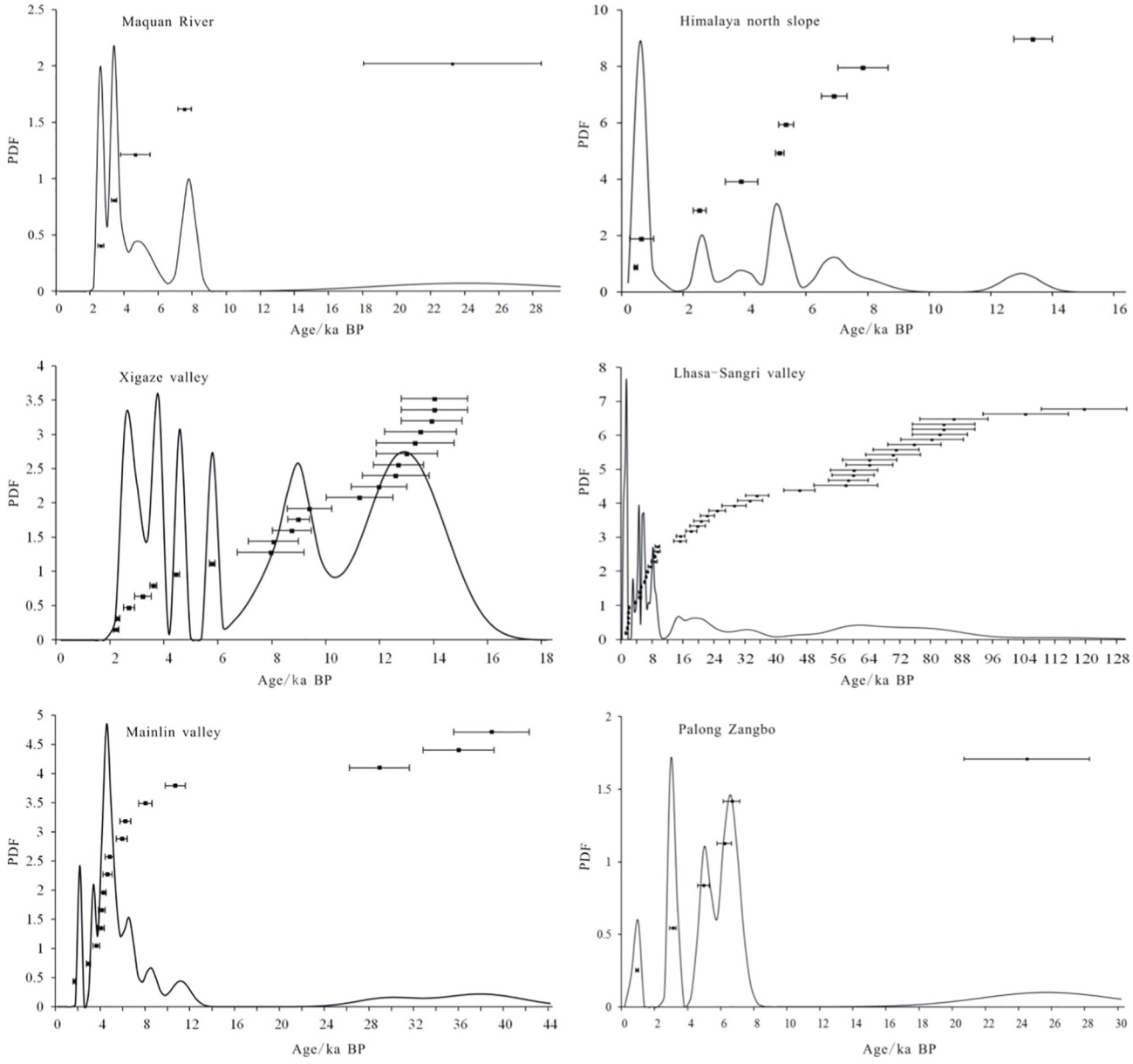

Fig. 8. Probability density functions (PDFs) of eolian sediment ages in different regions of the YTR catchment. See Fig. 1 for locations.

Moreover, in the Holocene the influence of the ASM extended to the Nyainqentanglha Mountains and other areas to the north of the YTR (Bird et al., 2014). Hence, since the LGM the paleoclimatic environment of the YTR basin has been within the sphere of influence of the ASM, which suggests that the eolian depositional response in the valley should be related to the paleoclimate of the larger region and provide a record of the interplay between the ASM, insolation, and the westerlies.

As discussed above, the PDF of eolian sediment ages in the YTR catchment shows an increase in eolian deposition between the LGM and the YD (Fig. 9A). Trends in the paleoclimate indicators (Fig. 9B–E) suggest warmer and wetter conditions, with increase in mean effective paleo-moisture from the Asia monsoon margin (Herzschuh, 2006), increase in summer insolation at 30°N (Berger and Loutre, 1991), and less negative $\delta^{18}O$ content in the Greenland GRIP record (Johnsen et al., 2001). Eolian deposition in the YTR catchment at this time seems contrary to the wetter conditions, although it is supported by the increased terrigenous material as indicated by reduced reflectance of Arabian Sea sediment (Deplazes et al., 2013) (Fig. 9E). In the YD period, there is good correspondence between eolian deposition in YTR and low average effective moisture in central Asia and the cold climate period recorded by the Greenland ice sheet, which may be indicative of enhanced westerlies. In the Holocene warm period, c. 8–5 ka BP (Shaun et al., 2013), there is strong development of eolian deposition in the YTR basin that seems to be contrary to the warm and wet regional climate scenario (Dong et al., 2017a). However, the strong solar radiation that intensifies the ASM pushes the subtropical high northward and the precipitation center is toward the northern plateau, leading to a decrease in precipitation in the YTR catchment. Thus, the extensive development of eolian deposits in the valley at this time is not indicative of regional aridity, but rather a signal of an intensified ASM. In addition, after the strong ASM crosses the great cold source of the Himalayas, it creates a strong downdraft in the YTR valley (the "foehn effect") that enhances aridity, and may contribute to eolian sediment accumulation. Accordingly, eolian deposition in the YTR basin is indicative of different paleoclimate scenarios in different periods. In addition to global climate, eolian sediments developed in alpine valley environments are

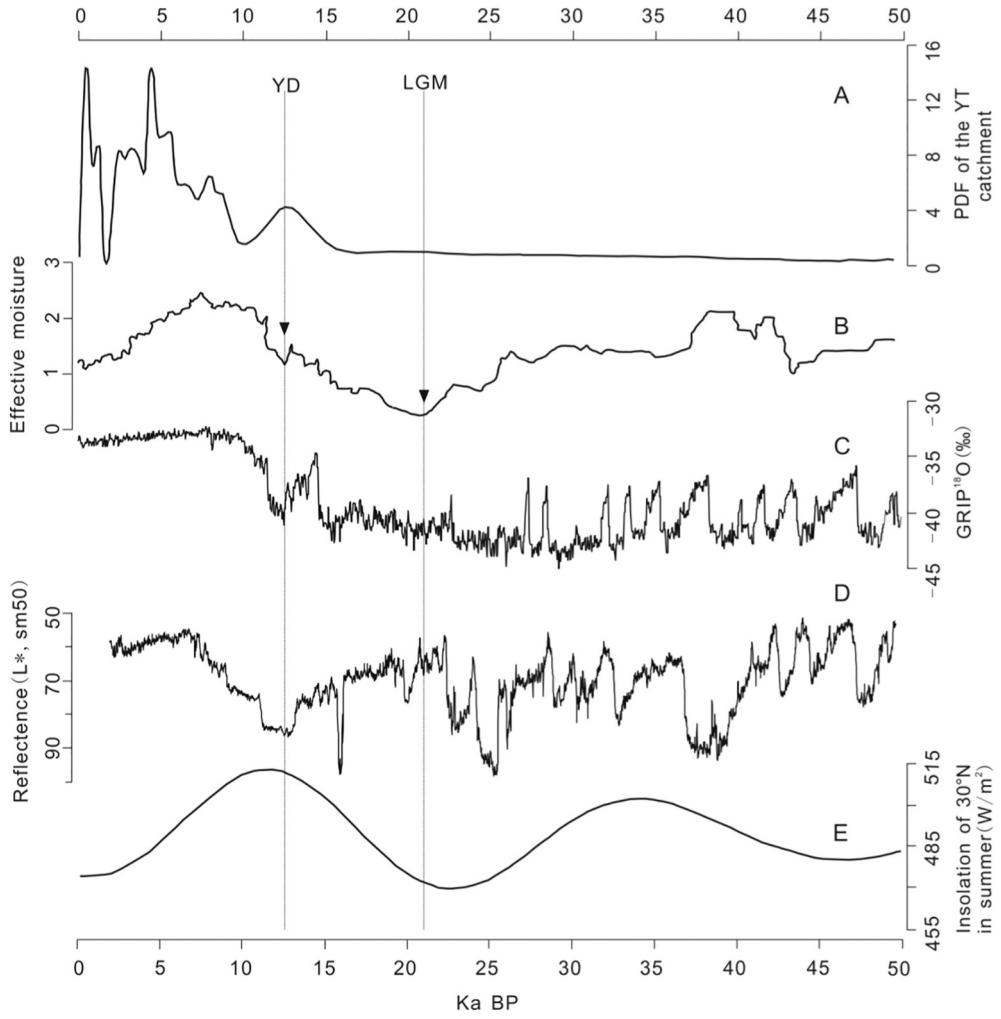

Fig. 9. Comparison of the probability density function (PDF) of eolian sediment ages for the YTR catchment since 50 ka BP with various indicators of paleoclimate. (A) PDF of eolian sediment ages from the YTR catchment; (B) Mean effective paleo-moisture from the Asian monsoon margin (Herzschuh, 2006); (C) GRIP $\delta^{18}O$ record from Greenland (Johnsen et al., 2001); (D) Arabian Sea reflectance (Deplazes et al., 2013); (E) Insolation at 30° N (Berger and Loutre, 1991). The Younger Dryas (YD) and Last Glacial Maximum (LGM) are marked on the graphs.

controlled by many local environmental factors, and the connection to global and regional events may be modified by local responses to these changes.

6. Conclusions

Thirty new OSL ages are combined with 72 previously published ages in an analysis the response of eolian accumulation to paleoenvironmental changes. Eolian sediment ages from profiles spread across the YTR catchment range from 0.4 ± 0.1 ka BP to at least 84.6 ± 8.7 ka (possibly as old as 118 ± 11 ka BP), but most fall in the period between the late glacial (15 ka BP) and little ice age. Eolian deposits older than the LGM are rare in the YTR catchment, which is consistent with other areas on the TP, and may be related to the overall erosional environment. A large amount of lacustrine and alluvial/fluvial clastic supply may have been the main controlling factor on eolian accumulation in the YTR catchment after the LGM. Dates of eolian sediment accumulation vary in different reaches of the YTR catchment, suggesting that factors governing the processes of eolian deposition vary across the catchment, causing inherent spatial-temporal disparities. And the presence of lacustrine and eolian sediments of similar ages shows that different types of sedimentary environments may co-exist in geologic periods in the different parts of the YTR catchment, depending on local conditions.

In different parts of the YTR catchment, there are widely developed accumulations of sandy loess, eolian sand, and other wind-generated deposits that are not indicative of climatic aridity. In short, eolian deposition in the YTR basin is controlled by the regional environment and global paleoclimate, which has no a simple correspondence between the eolian accumulation and global changes. And the connection to global and regional events may be modified by local responses to these changes.

Acknowledgments

This research was financially supported by the Second Tibetan Plateau Scientific Expedition and Research Program (STEP) (Grant nos. 2019QZKK0602 and 2019QZKK0805), the National Key Research and Development Program of China (Grant no. 2018YFC0406605), and the Qinghai Provincial Science and Technology Innovation Platform (Grant nos. 2018-ZJ-T03, 2018-ZJ-T10). We are thankful to two anonymous reviewers for their constructive comments on a previous version of the manuscript.

References

Aitken, M.J., 1998. An Introduction to Optical Dating: The Dating of Quaternary Sediments by the Use of Photon-stimulated Luminescence. Oxford University Press, Oxford, pp. 5–15.
Berger, A., Loutre, M.F., 1991. Insolation values for the climate of the last 10 million years. Quat. Sci. Rev. 10 (4), 297–317. https://doi.org/10.1016/0277-3791(91)90033-Q.

Bird, B.W., Polisar, P.J., Lei, Y.B., Thompson, L.G., Yao, T.D., Finney, B.P., Bain, D.J., Pompeani, D.P., Steinman, B.A., 2014. A Tibetan lake sediment record of Holocene Indian summer monsoon variability. Earth Planet. Sci. Lett. 399, 92–102. https://doi.org/10.1016/j.epsl.2014.05.017.

Böhner, J., 2006. General climatic controls and topoclimatic variations in central and high Asia. Boreas 35, 279–295. https://doi.org/10.1111/j.1502-3885.2006.tb01158.x.

Chase, B., 2009. Evaluating the use of dune sediments as a proxy for palaeo-aridity: a southern African study. Earth Sci. Rev. 93 (1–2), 31–45. https://doi.org/10.1016/j.earscirev.2008.12.004.

Chen, F.H., Wu, D., Chen, J.H., Zhou, A.F., Yu, J.Q., Shen, J., Wang, S.M., Huang, X.Z., 2016. Holocene moisture and East Asian summer monsoon evolution in the northeastern Tibetan Plateau recorded by Lake Qinghai and its environs: a review of conflicting proxies. Quat. Sci. Rev. 154, 111–129. https://doi.org/10.1016/j.quascirev.2016.10.021.

Deplazes, G., Lückge, A., Peterson, L.C., Timmermann, A., Hamann, Y., Hughen, K.A., Röhl, U., Laj, C., Cane, M.A., Sigman, D.M., Haug, G.H., 2013. Links between tropical rainfall and North Atlantic climate during the last glacial period. Nat. Geosci. 6 (3), 213–217. https://doi.org/10.1038/NGEO1712.

Dong, Z.B., Hu, G.Y., Qian, G.Q., Lu, J.F., Zhang, Z.C., Luo, W.Y., Lyu, P., 2017a. High-Altitude aeolian research on the Tibetan Plateau. Rev. Geophys. 55, 864–901. https://doi.org/10.1002/2017RG000585.

Dong, Z.B., Lu, J.H., Qian, G.Q., Lyu, P., Luo, W.Y., Zhang, Z.S., 2017b. Tibetan Plateau Altas of Aeolian Geomorphology. Xi'an Map Publishing House, Xi'an, pp. 1–91 (Billingual in Chinese and English).

Du, S.S., Wu, Y.Q., Tan, L.H., Huang, W.M., Hao, C.Z., 2018. Geochemical characteristics of fine and coarse fractions of sediments in the Yarlung Zangbo river basin (southern Tibet, China). Environ. Earth Sci. 77, 336–347. https://doi.org/10.1007/s12665-018-7468-5.

Herzschuh, U., 2006. Palaeo-moisture evolution in monsoonal Central Asia during the last 50,000 years. Quat. Sci. Rev. 25 (1–2), 163–178. https://doi.org/10.1016/j.quascirev.2005.02.006.

Hou, J.Z., William, J.D., Wang, M.D., He, Y., Liang, J., 2017. Influence of the Indian monsoon and the subtropical jet on climate change on the Tibetan Plateau since the late Pleistocene. Quat. Sci. Rev. 163, 84–94. https://doi.org/10.1016/j.quascirev.2017.03.013.

Hu, H.P., Feng, J.L., Chen, F., 2018. Sedimentary records of a palaeo-lake in the middle Yarlung Tsangpo: Implications for terrace genesis and outburst flooding. Quat. Sci. Rev. 192, 135–148. https://doi.org/10.1016/j.quascirev.2018.05.037.

Jin, H.L., Dong, G.R., Liu, Y.Z., Zhang, C.L., 1998. The sand field evolution and climatic changes in the middle course area of Yarlung Zangbo river in Tibet, China since 0.8 Ma BP. J. Desert Res. 18 (2), 97–104 (in Chinese with English abstract).

Jin, H.L., Dong, G.R., Gao, S.Y., Zhang, C.L., 2000. Environmental and south-western monsoonal changes in the middle Tibetan Plateau since 300 ka BP. J. Desert Res., 20 (3), 234-237 (in Chinese with English abstract). Quat. Geochronol. 48, 171–179. https://doi.org/10.1016/j.quageo.2018.10.001.

Jin, J.H., Li, Z.Z., Huang, Y.M., Fan, X.C., Jiang, F., Cheng, Y., Xu, X.L., Ling, Z.Y., Liu, X.M., 2018. Chronology of a late Neolithic site along the coast of the east China sea Quat. Geochronol 2000, 171–179.

Johnsen, S.J., Dahl-Jensen, D., Gundestrup, N., Steffensen, J.P., Clausen, H.B., Miller, H., Masson-Delmotte, V., Sveinbjörnsdottir, A.E., White, J., 2001. Oxygen isotope and palaeotemperature records from six Greenland ice-core stations: Camp Century, Dye-3, GRIP, GISP2, Renland and North GRIP. J. Quat. Sci. 16 (4), 299–307. https://doi.org/10.1002/jqs.622.

Kaiser, K., Lai, Z.P., Schneider, B., Reudenbach, C., Miehe, G., Brückner, H., 2009. Stratigraphy and palaeoenvironmental implications of Pleistocene and Holocene aeolian sediments in the Lhasa area, southern Tibet (China). Palaeogeogr. Palaeoclimatol. Palaeoecol. 271 (3–4), 329–342. https://doi.org/10.1016/j.palaeo.2008.11.004.

Kaiser, K., Lai, Z.P., Schneider, B.Junge, 2010. Late Pleistocene genesis of the middle Yarlung Zhangbo Valley, southern Tibet (China), as deduced by sedimentological and luminescence data. Quat. Geochronol. 5 (2–3), 200–204. https://doi.org/10.1016/j.quageo.2009.01.005.

Kumar, A., Srivastava, P., Meena, N.K., 2017. Late Pleistocene aeolian activity in the cold desert of Ladahk: a record from sand ramps. Quat. Int. 443, 13–28. https://doi.org/10.1016/j.quaint.2016.04.006.

Lai, Z.P., Brückner, H., 2008. Effects of feldspar contamination on equivalent dose and the shape of growth curve for OSL of silt-sized quartz extracted from Chinese loess. Geochronometria 30 (1), 49–53. https://doi.org/10.2478/v10003-008-0010-0.

Lai, Z.P., Kaiser, K., Bruckner, H., 2009. Luminescence-dated aeolian deposits of late Quaternary age in the southern Tibetan Plateau and their implications for landscape history. Quat. Res. 72 (3), 421–430. https://doi.org/10.1016/j.yqres.2009.07.005.

Lancaster, N., 2008. Desert dune dynamics and development: insights from luminescence dating. Boreas 37 (4), 559–573. https://doi.org/10.1111/j.1502-3885.2008.00055.x.

Lancaster, N., Yang, X.P., Thomas, D., 2013. Spatial and temporal complexity in Quaternary desert datasets: implications for interpreting past dryland dynamics and understanding potential future changes. Quat. Sci. Rev. 78, 301–302. https://doi.org/10.1016/j.quascirev.2013.07.018.

Lehmkuhl, F., Klinge, M., Rees-Jones, J., Rhodes, E.J., 2000. Late Quaternary aeolian sedimentation in central and south-eastern Tibet. Quat. Int. 68–71, 117–132. https://doi.org/10.1016/S1040-6182(00)00038-0.

Li, S., Wang, Y., Erdun, H.S., Yang, P., Jin, H.L., Zhang, J.K., 1997. Classification and development of aeolian sand landform in the Yurlung Zangbo valley. J. Desert Res. 17 (4), 342–350 (in Chinese with English abstract).

Li, S., Dong, G.R., Shen, J.Y., Yang, P., Liu, X.W., Wang, Y., Jin, H.L., Wang, Q., 1999. Formation mechanism and development pattern of aeolian sand landform in Yarlung Zangbo river valley. Sci. China Earth Sci. 42 (3), 272–284.

Li, C.L., Kang, S.C., Zhang, Q.G., Wang, F.Y., 2009. Rare earth elements in the surface sediments of the Yarlung Tsangpo (Upper Brahmaputra River) sediments. southern Tibetan Plateau. Quat. Int. 208 (1–2), 151–157. https://doi.org/10.1016/j.quaint.2009.05.003.

Li, Q., Zhang, C.L., Shen, Y.P., Wenru, J., Li, J., 2016. Developing trend of aeolian desertification in China's Tibet Autonomous region from 1977 to 2010. Environ. Earth Sci. 75, 894–905. https://doi.org/10.1007/s12665-016-5709-z.

Ling, Z.Y., Chen, L., Lu, B.L., Wang, J.P., Chen, F.H., 2018. Chronology and provenance of the nebkhas around salt lakes in the Qaidam basin and their environmental implication. Quat. Sci. 38 (3), 611–622 (in Chinese with English abstract). 10.11928/j.issn.1001-7410.2018.03.06.

Ling, Z.Y., Jin, J.H., Wu, D., Liu, X.J., Xia, D.S., Chen, F.H., 2019. Aeolian sediments and their paleoenvironmental implication in the Yarlung Tsangpo catchment (southern Tibet, China) since MIS3. Acta Geograph. Sin. 74 (11), 2385–2400 (in Chinese with English abstract). 10.11821/dlxb201911014.

Liu, W.M., Lai, Z.P., Hu, K.H., Ge, Y.G., Cui, P., Zhang, X.G., Liu, F., 2015. Age and extent of a giant glacial-dammed lake at Yarlung Tsangpo gorge in the Tibetan Plateau. Geomorphology 246, 370–376. https://doi.org/10.1016/j.geomorph.2015.06.034.

Mason, J.A., Nater, E.A., Zanner, C.W., Bell, J.C., 1999. A new model of topographic effects on the distribution of loess. Geomorphology 28 (3–4), 223–236. https://doi.org/10.1016/S0169-555X(98)00112-3.

Murray, A.S., Wintle, A.G., 2000. Luminescence dating of quartz using an improved single-aliquot regenerative-dose protocol. Radiat. Meas. 32 (1), 57–73. https://doi.org/10.1016/S1350-4487(99)00253-X.

Pan, B., Hu, X., Gao, H., Hu, Z., Cao, B., Geng, H., Li, Q., 2013. Late Quaternary river incision rates and rock uplift pattern of the eastern Qilian Shan mountain, China. Geomorphology 184, 84–97. https://doi.org/10.1016/j.geomorph.2012.11.020.

Prescott, J.R., Hutton, J.T., 1994. Cosmic ray contributions to dose rates for luminescence and ESR dating: large depths and long-term time variations. Radiat. Meas. 23 (2–3), 497–500. https://doi.org/10.1016/1350-4487(94)90086-8.

Roskin, J., Tsoar, H., Porat, N., Blumberg, D.G., 2011. Palaeoclimate interpretations of late Pleistocene vegetated linear dune mobilization episodes: evidence from the northwestern Negev dunefield, Israel. Quat. Sci. Rev. 30 (23–24), 3364–3380. https://doi.org/10.1016/j.quascirev.2011.08.014.

Shaun, A.M., Jeremy, D.S., Peter, U.C., Alan, C.M., 2013. A reconstruction of regional and global temperature for the past 11300 years. Science 339 (6124), 1021–1198. https://doi.org/10.1126/science.1228026.

Shen, W.S., Li, H.D., Sun, M., Yang, S.G., Zhang, Q., 2010. Evolution of aeolian sand in the source region of China's Yarlung Zangbo river. Environ. Sci. Technol. 2, 344–351.

Shen, W.S., Li, H.D., Sun, M., Jiang, J., 2012. Dynamics of aeolian sandy land in the Yarlung Zangbo river basin of Tibet, China from 1975 to 2008. Glob. Planet. Chang. 86–87, 37–44.

Singhvi, A.K., Bluszcz, A., Bateman, M.D., Rao, M.S., 2001. Luminescence dating of loesspalaeosol sequences and coversands: methodological aspects and palaeoclimatic implications. Earth Sci. Rev. 54 (1–3), 193–211. https://doi.org/10.1016/s0012-8252(01)00048-4.

Smalley, I., O'Hara-Dhand, K., Kwong, J., 2014. China: materials for a loess landscape. Catena 117, 100–107. https://doi.org/10.1016/j.catena.2013.11.016.

Stauch, G., Pötsch, S., Zhao, H., Lehmkuhl, F., 2014. Interaction of geomorphological processes on the north-eastern Tibetan Plateau during the Holocene, an example from a sub-catchment of lake Donggi Cona. Geomorphology 210, 23–35. https://doi.org/10.1016/j.geomorph.2013.12.014.

Stauch, G., 2015. Geomorphological and palaeoclimate dynamics recorded by the formation of aeolian archives on the Tibetan Plateau. Earth Sci. Rev. 150, 393–408. https://doi.org/10.1016/j.earscirev.2015.08.009.

Sun, J.M., Li, S.H., Muhs, D.R., Li, B., 2007. Loess sedimentation in Tibet: provenance, processes, and link with Quaternary glaciations. Quat. Sci. Rev. 26 (17–18), 2265–2280. https://doi.org/10.1016/j.quascirev.2007.05.003.

Tarasov, L., Peltier, W.R., 2005. Arctic freshwater forcing of the Younger Dryas cold reversal. Nature 435 (7042), 662–665. https://doi.org/10.1038/nature03617.

Telfer, M.W., Thomas, D.S.G., 2007. Late Quaternary linear dune accumulation and chronostratigraphy of the southwestern Kalahari: implications for aeolian palaeoclimatic reconstructions and predictions of future dynamics. Quat. Sci. Rev. 26 (19–21), 2617–2630. https://doi.org/10.1016/j.quascirev.2007.07.006.

Wang, P., Scherler, D., Liu-Zeng, J., Mey, J., Avouac, J.P., Zhang, Y., Shi, D., 2014. Tectonic control of Yarlung Tsangpo gorge revealed by a buried canyon in southern Tibet. Science 346 (6212), 978–981. https://doi.org/10.1126/science.1259041.

Yang, Y.S., 1984. Aeolian landform on the banks of river valley-case study in Yalu Tsangpo river valley. J. Desert Res. 4 (3), 12–16 (in Chinese with English abstract).

Yang, Y.S., Li, B.Y., Yin, Z.S., Zhang, Q.S., 1982. The formation and evolution of landforms in the Xizang Plateau. Acta Geograph. Sin. 37 (1), 76–87 (in Chinese with English abstract). 10.11821/xb198201009.

Yao, T.D., Thompson, L., Yang, W., 2012. Different glacier status with atmospheric circulations in Tibetan Plateau and surroundings. Nat. Clim. Chang. 2, 663–667. https://doi.org/10.1038/nclimate1580.

Zhang, D.D., Li, S.H., 2002. Optical dating of Tibetan human hand- and footprints: an implication for the palaeoenvironment of the last glaciations of the Tibetan Plateau. Geophys. Res. Lett. 29 (5), 9–11. https://doi.org/10.1029/2001GL013749.

Zhou, N., Zhang, C.L., Wu, X.X., Wang, X.M., Kang, L.Q., 2014. The geomorphology and evolution of aeolian landforms within a river valley in a semi-humid environment: a case study from Mainling valley, Qinghai-Tibet Plateau. Geomorphology 224, 27–38. https://doi.org/10.1016/j.geomorph.2014.07.012.